Bioactive Materials 10 (2022) 269–280

Contents lists available at ScienceDirect

Bioactive Materials

journal homepage: www.keaipublishing.com/en/journals/bioactive-materials

Experimental study of a 3D printed permanent implantable porous Ta-coated bone plate for fracture fixation

Baoyi Liu [1], Zhijie Ma [1], Junlei Li, Hui Xie, Xiaowei Wei, Benjie Wang, Simiao Tian, Jiahui Yang, Lei Yang, Liangliang Cheng, Lu Li, Dewei Zhao [*]

Orthopaedic of Department, Affiliated ZhongShan Hospital of Dalian University, Dalian, 116001, China

ARTICLE INFO

Keywords:
3D printing
Porous bone plate
Ta coating
Osteogenesis
Osseointegration

ABSTRACT

Metal plates have always been the gold standard in the clinic for internal fracture fixation due to their high strength advantages. However, high elastic modulus can cause stress shielding and lead to bone embrittlement. This study used an electron beam melting method to prepare personalized porous Ti6Al4V (pTi) bone plates. Then, chemical vapor deposition (CVD) technology coats tantalum (Ta) metal on the pTi bone plates. The prepared porous Ta-coated bone plate has an elastic modulus similar to cortical bone, and no stress shielding occurred. In vitro experiments showed that compared with pTi plates, Ta coating significantly enhances the attachment and proliferation of cells on the surface of the scaffold. To better evaluate the function of the Ta-coated bone plate, animal experiments were conducted using a coat tibia fracture model. Our results showed that the Ta-coated bone plate could effectively fix the fracture. Both imaging and histological analysis showed that the Ta-coated bone plate had prominent indirect binding of callus formation. Histological results showed that new bone grew at the interface and formed good osseointegration with the host bone. Therefore, this study provides an alternative to bio-functional Ta-coated bone plates with improved osseointegration and osteogenic functions for orthopaedic applications.

1. Introduction

Fractures in weight-bearing parts of a skeleton require internal fixation. The current internal fixation is mainly made of metal materials and degradable materials. However, the elastic modulus of metal materials (such as stainless steel, Ti and its alloys) is too different from that of human bone tissue [1–3]. The mismatch of a high elastic modulus and bone biomechanics will have a negative impact on callus formation and fracture healing, even requiring a second operation [4,5]. In addition, degradable internal fixation cannot be used in load-bearing fractures due to its poor mechanical properties [6]. Therefore, the development of an internal fixation system that does not require a second operation for removal has been a research hotspot in the orthopaedics community for many years [7,8]. To reduce the elastic modulus of metal materials, researchers have carried out research studies on porous medical metal implant materials [9]. The common materials are pTi and so on [10]. As a porous implant material used for bone tissue trauma and defect treatment, its porosity should reach 30 ~ 85%, and the pores are preferably all connected and evenly distributed, or part of the pores are connected and evenly distributed according to the needs, so that the material can be connected to the human body [9,11]. Furthermore, the growth of the bone tissue should be consistent, and the weight of the material itself should be reduced so that it is suitable for human implantation. These porous materials only reduce the weight and the stress shielding effect on the basis of traditional materials, but they do not make a qualitative change to the material itself.

In recent years, Ta metal has attracted much attention from scholars due to its excellent biological activity [12–14]. Because the density and elastic modulus of pure Ta are too high, it is not beneficial for use as a lightweight implanted device or the comfort of patient movement after implantation, and its clinical application is limited [10]. The emergence of porous Ta metal solves the above problems. After long-term clinical observation, porous Ta implant devices show excellent biocompatibility in the body, and it is similar to the interconnected microporous structure

Peer review under responsibility of KeAi Communications Co., Ltd.
* Corresponding author. No.6 Jiefang Street, Dalian, Liaoning, 116001, China.
E-mail address: zhaodewei2016@163.com (D. Zhao).
[1] The first two authors contributed equally to this article.

https://doi.org/10.1016/j.bioactmat.2021.09.009
Received 27 June 2021; Received in revised form 25 August 2021; Accepted 4 September 2021
Available online 16 September 2021

of the trabecular bone structure [15,16]. This helps more new bone grow into the implant after implantation and provides greater long-term stability [17–21]. However, the relatively high manufacturing cost and the incapability to produce customized implants using medical image data have limited its widespread application.

Based on the above research, our team has developed a porous internal fixation system that can be used for weight-bearing fractures and has the ability to promote bone growth and bone ingrowth. First, 3D printing technology was used to prepare pTi bone plates, and then CVD technology was used to coat bioactive Ta metal on pTi bone plates. It is expected that a relatively ideal metal bone plate can be prepared, which can not only avoid stress shielding but also, with excellent biological activity, can be permanently implanted in the body without the need for surgical removal. At the same time, a goat animal model of a tibia fracture was constructed to evaluate the internal fixation of porous Ta-coated bone plates, and the changes in osteogenic factors and cells involved in bone formation around the bone plate during fracture healing were explained. We hope to provide a new type of bone plate with potential for the treatment of fractures.

2. Materials and methods

2.1. Preparation of pTi bone plate

According to the non-fracture-side bone computed tomography (CT) data, Auto CAD, Pro E, and Magics software were used to design and obtain a 3D geometric model of pTi bone plates mimicking trabecular bone in format. Using Ti6Al4V ELI spherical powder as raw material, a pTi metal bone plate with imitative trabecular structure was prepared, and printed under protective argon atmosphere. The parameters of the 3D printing process were powder spreading thickness of 30 μm, and laser power of 150 W. The exposure time was 40 μs, the spot pitch was 50 μm, and the line pitch was 60 μm. The as-fabricated samples were placed in a sand blaster to remove metallic powders that had adhered to the surface. Then, the samples were rinsed with acetone, ethanol and distilled water successively in an ultrasonic cleaner for 15 min and then air-dried.

2.2. Preparation of porous Ta coating bone plate

A CVD technique was used to prepare the Ta coating on the surface of the aforementioned pTi bone plate. First, the pTi bone plate and the Ta raw materials were placed at both ends of the reaction chamber. When the degree of vacuum dropped below 133Pa, the chlorine gas was delivered to the front end of the chlorination chamber heated to 1050 °C. The chlorine gas first reacted with the Ta raw material to form $TaCl_5$. Then, the hydrogen gas reacted with $TaCl_5$ to form Ta, which was deposited on the pTi bone plate. 2 times of deposition, 7 h each time, the total deposition time was 14 h. After a new Ta coated pTi bone plate was successfully prepared, all samples were ultrasonically cleaned.

2.3. Characterization

Scanning electron microscopy (SEM, Hitachi SU-3500) was used to analyse the micromorphology, elemental composition, and thickness of the Ta coating. The crystal structure of the coating was identified using an X-ray diffraction (XRD, Empyrean-100). The diffraction patterns were collected with Cu Kα radiation over a 2θ range of 20° ~ 100°. The scratch test characterizing the mechanical properties of Ta coatings was performed in Scratch Test System (Anton Paar Instruments). A linearly progressive normal load was applied with a Rockwell (diamond) indenter of 200 μm radius. The test was conducted in the 0.3 ~ 40 N load range with a loading rate of 100 mN/min. To allow total delamination to occur within the scratch span, a scratch length of 4 mm was selected. The critical normal force (critical load) at which adhesive failure was first detected (with a sudden change in friction forces) was used as a measure of adhesion. We used Ta coated solid Ti substrates for the XRD and scratch analyses instead of Ta coated pTi scaffolds. The mechanical property tests of the bone plates were conducted on a universal testing machine (Instron-5900, Instron). All mechanical tests were repeated three times.

2.4. Biomechanical tests

A three-point bend test was used to evaluate the bending strength of the bone plates, and was tested in accordance with the ISO 9585:1990 standard [22]. The bone plates were positioned on the same horizontal plane on two lower stabilizing points positioned 30 mm apart. One upper moving point was positioned at the center of the two lower points. The loading speed is 5 mm/min. The bending strength of the bone plates was obtained from the average of three test samples. Three tensile test samples of the bone plates were tested to determine the mechanical properties. Tensile tests were performed at a strain rate of 1 mm/min. Displacements were measured using an extensometer with a 25 mm gauge length. Yield stress and Young's modulus were determined according to ISO 18437–5:2011 [23].

2.5. In vitro biocompatibility

Human osteoblasts (MG-63) (Beijing Union Cell Bank) were used to evaluate the cytocompatibility of the Ta coating. MG-63 cells were cultured in a medium alpha (α-MEM, Hyclone, USA) containing 10% fetal bovine serum (FBS, Corning, USA) at 37 °C in a 5% CO_2 incubator. The cell suspension (25 μl) was seeded on the Ta-coated solid Ti6Al4V substrates at a concentration of 5×10^4 cells/ml. After culturing for 3 days and 7days, the non-adherent cells were discarded along with the culture medium. The sample was washed twice with PBS, dehydrated continuously, then dried and sprayed with gold. Next, the growth of MG-63 cells was observed on the Ta-coated solid Ti substrates material using a scanning electron microscope (Hitachi SU-3500).

2.6. In vivo animal studies

2.6.1. Experimental animals and materials

Forty-eight goats of both sexes weighing 30 ~ 35 kg and aged 2 years were obtained from Dalian Medical University. The animal certificate number was SCX (Liao) 20150015. The bone plate specifications are as follows: 7-pore titanium-limited contact compression plates (dimensions of 80 mm × 12 mm × 3 mm, screw diameter of 3.5 cm, and screw length of 16 ~ 24 mm) were obtained from Weigo Orthopedics Co. Ltd. (Weihai, Shandong, China). Porous metallic bone plates (3D printed 7-pore biological titanium plates with dimensions of 80 mm × 12 mm × 3 mm) were obtained from the Orthopedics Medical Research Center at Dalian University. CVD was used to evenly deposit tantalum on 3D-printed 7-pore titanium plates to generate porous Ta-coated plates. Ta-coated screws were produced from Ti screws (diameter of 3.5 cm and length of 16 ~ 24 mm; obtained from Weigo Orthopedics Co. Ltd, Weihai, Shandong, China) by CVD technology in the Orthopedics Medical Research Center at Dalian University. According to differences in mechanical strength requirements, we set the tantalum coating thickness to 50 μm for the porous plates in the animal experiments and the clinical trials with patients. Approval was obtained from the Institutional Animal Care and Use Committee before study initiation (ethics committee permission number 2016–120). All animals were randomized into 3 groups with 16 animals per groups. These groups were the conventional Ti plate control groups (n = 16), pTi plate control groups (n = 16), and porous Ta-coated plate groups (n = 16).

2.6.2. Surgery procedures

All animals underwent transverse osteotomy at the left tibia. The osteotomy site, anaesthesia method, surgery method, fixation method, equipment, and surgical staff were all identical. Ketamine and

Sumianxin were mixed in a 2:1 ratio, and 0.5 mL/kg was administered intramuscularly for anaesthesia. Subsequently, a 10 cm-long longitudinal incision was made at the anterolateral skin of the middle tibia. Subcutaneous tissues and deep fascia were incised, and blunt separation of the muscles was carried out to expose the shaft of the tibia. A steel ruler was used to measure the full length of the tibia and confirm its midpoint. An annular incision was made at this site, and approximately 2 mm of periosteum was removed. A wire saw was used for transverse osteotomy at this site to create a 2 mm-wide bone defect. Conventional Ti, pTi bone plates and screws, or porous Ta-coated bone plates and Ta-coated screws were used to fix the fracture at the lateral tibia. Three screws, each of appropriate lengths, were implanted at the two ends of the fracture, taking note to retain 2 mm of fracture space. This step was followed by haemostasis, rinsing of the surgical site with physiological saline, and suturing of the deep fascia and skin incision. After surgery, non-weight-bearing braces were worn, and the goats were allowed to roam around normally. Routine dressing changes were administered to the wound until recovery. Penicillin sodium (800,000 U/d) was injected 30 min before surgery and 3 days after surgery to prevent infection.

2.6.3. X-ray assessment of the fracture healing status

Immediately and at 4, 8, 12, and 16 weeks after surgery, the animals were anaesthetized, and the treated limb was placed on an X-ray machine. Professional staff then took anteroposterior and lateral X-rays. The imaging conditions were as follows: distance of 100 cm, voltage of 60 kV, exposure time of 0.0025 s, and current of 500 mA. The development and fixation times for each X-ray film were strictly consistent. The Lane-Sandhu scores were used to evaluate the callus formation rate and visible level of the fracture line to evaluate the bone healing time of the fractures in each groups.

2.6.4. Micro-CT observations

Three groups of goats underwent high-resolution scanning of all tibia samples, which were taken from each groups at 4, 8, 12, and 16 weeks after surgery using a micro-CT scanner from Siemens Medical Solutions (USA, Siemens Inc). The radiographic data were collected and reconstructed with the Inveon Acquisition Workplace (USA, Siemens Inc.), and the Inveon Research Workplace (USA, Siemens Inc.) was used to analyse the data. The scanning protocol used was 80 kV and 500 μA, and the effective pixel size was 28.21 μm. Three-dimensional reconstruction of the volume of interest (VOI) in these regions was carried out, and the radiographic images and CT grey values were analysed to evaluate fracture healing and bone strengthening. General analysis was used to obtain coronal-plane, sagittal-plane and horizontal-plane images. Multimodal 3D visualization was used to obtain a stereoscopic image of the fracture and bone plate region.

2.6.5. Gross morphology observation and histological staining

After the biomechanical tests were completed, the soft surface tissue at the fracture site in the goat tibias was examined. The volume of the callus at the fracture site was observed before the fracture site was cut open longitudinally in a symmetrical manner for observation of the callus connection status and bone stem medullary patency status. After the samples were embedded in paraffin and sectioned, Van-Gieson staining was carried out. Histological changes in the callus were observed under a microscope at different times after the fracture.

2.6.6. Methodological assessment of acid-etching for visualizing osteocytes around bone plates via SEM

The goat tibias were harvested during the necropsy, wrapped in saline-soaked gauze, and then frozen at −20 °C until analysis. The femurs were thawed to room temperature, and plate segments were isolated by making parallel buccal-lingual cuts using a diamond-coated band saw. Each segment was then processed for embedment in methyl methacrylate (MMA; Aldrich) using standard methods. Following dehydration in a graded series of ethanol (70%, 95%, and 100%) for 4 h each, the specimens were cleared with xylene (4 h) and then infiltrated with MMA under vacuum for 24 h. The specimens were transferred to a solution of MMA +3% dibutyl phthalate (DBP; Sigma-Aldrich) under vacuum for 3 days. The specimens were then embedded in MMA + DBP +0.25% catalyst at room temperature; polymerization occurred within 7 days. After polymerization, 5-mm thick coronal slices were cut using a diamond wire saw. One face of the slice was polished. The polished section faces were acid-etched using standard methods. Immediately following etching, each section was immersed with the polished face up in sodium hypochlorite (bleach) for 5 min followed by a brief, 2-s slow-agitated rinse (by hand) in dH_2O. The sections were placed in a desiccator overnight to completely dry the specimen and then prepared for SEM. Specimens were mounted on aluminium discs using double-sided tape. The edge of each section was painted with colloidal silver paste at the union between the plastic of the specimen and aluminium to aid in the conduction of the specimen. Specimens were sputter coated with 3 ~ 5 nm of gold palladium at 2.5 kV at 20 mA for 105 s with a Polaron E5000S, and then the samples were viewed on a JSM JEOL-6390LV scanning electron microscope operated at an accelerating voltage of 5 kV. The osteocytes around the plate were qualitatively evaluated.

2.6.7. Immunohistochemistry

The sections were placed in a 60 °C oven for 2 h before immersion for 5 min in xylene I, xylene II, 100% ethanol, 95% ethanol, 85% ethanol, and 75% ethanol sequentially. After 3 min of antigen retrieval in a high-pressure cooker, the steam was released, and the section was removed after 10 min and washed with PBS. The entire tissue was covered with two primary antibodies, one against vascular endothelial growth factor (VEGF; Biorbyt, orb13750) and one against bone morphogenetic protein 2 (BMP-2; Abcam, ab82511), and incubated overnight at 4 °C before the addition of secondary antibodies (Abcam). This addition was followed by 10 min of iron haematoxylin counterstaining and rinsing with water. Hydrochloric acid and ethanol were used for 30 s of differentiation before rinsing with water. Ammonium hydroxide solution was used for 3 min of bluing before rinsing with water. The sections were photographed, and the integrated optical density of the images was measured. Each test was performed in triplicate. A digital pathological image acquisition device was used for image acquisition, and Image-Pro Plus professional image software was used for quantitative analysis.

2.7. Finite element model and calculations

HyperWorks software (USA, Altair Inc.) was used to build a fracture model that was fixated together by a bone plate and six screws. The bone defect was 2 mm, and there were three types of bone plates: Ti plates, pTi plates and porous Ta-coated plates. Multiple cubic elements and their Boolean operations were used to simulate the damaged bones and the solid and porous plates. To improve the efficiency and accuracy of the analysis, a 1/4 symmetric model was used. The union conditions of different bone plates before and after fracture healing were set according to the results of the histological sections. Solid 185 elements were used to mesh the model, the elastic moduli of the Ti and bone were 104,000 MPa and 17,000 MPa, respectively, and the Poisson's ratio of the Ti was 0.3. A contact calculation was adopted, and the results adopted the von Mises criterion. In the analysis, the boundary condition was set as 0° of freedom in all directions at the bottom of the model, and the model was assumed to be in the normal stress position of the body, with an external load of 1000 N. Six models were established: Ti plate, pTi plate and porous Ta-coated plate fixation models before fracture healing and after fracture healing.

2.8. Statistical analysis

SPSS 20.0 statistics software was used for statistical analysis. The Shapiro-Wilk test was first used to determine whether the quantitative data followed a normal distribution. The Lane-Sandhu X-ray scores, the

maximum load in the three-point bending test, the maximum torque, the newly synthesized trabecular bone density, and the collagen levels were all found to be normally distributed data with homogeneity of variance. These results are expressed as the mean ± standard deviation. Multiple groups comparisons were carried out using one-way analysis of variance (ANOVA) or two-way repeated-measures ANOVAs over time as appropriate. If the difference was statistically significant, then the least significant difference (LSD) test method was used for comparison between two groups. A difference of $P < 0.05$ was deemed statistically significant.

3. Results

3.1. Surface characterization

Fig. 1 A1 shows the microscopic morphology of the 3D printed pTi bone plate, with a pore size of 600 ± 27 μm and a porosity of about 75%. Upon 1000 times magnification, it can be seen that the pTi surface was relatively smooth and flat (Fig. 1 A2). Fig. 1 B1 shows that the pTi surface contained a tight Ta coating, and the pTi substrate was completely covered by the Ta coating. The porous Ta-coated bone plate has a pore size of 550 ± 42 μm and a porosity of about 70%. Enlarging the Ta coating to 1000 times (Fig. 1 B2), it can be seen that the aggregation of Ta particles forms the Ta coating. The crystal grain structure is pyramidal, with uniform size, and the diameter is 5 ~ 15 μm. The Ta-coated bone plate was cut transversely (Fig. 1C1), and the thickness of the Ta coating was measured to be 53 μm (Fig. 1C2). Energy-dispersive X-ray spectroscopy (EDS) analysis results show that the surface element of the pTi bone plate was Ti6Al4V (Fig. 1 D1), and the surface element of the Ta-coated bone plate was Ta (Fig. 1 D2). The XRD pattern of the Ta coating on pTi is shown in Fig.l E. Typical peaks of Ta can be observed in the XRD pattern. All characteristic peaks were in good agreement with the JCPDS X-ray powder standards. The peaks corresponding to (110),

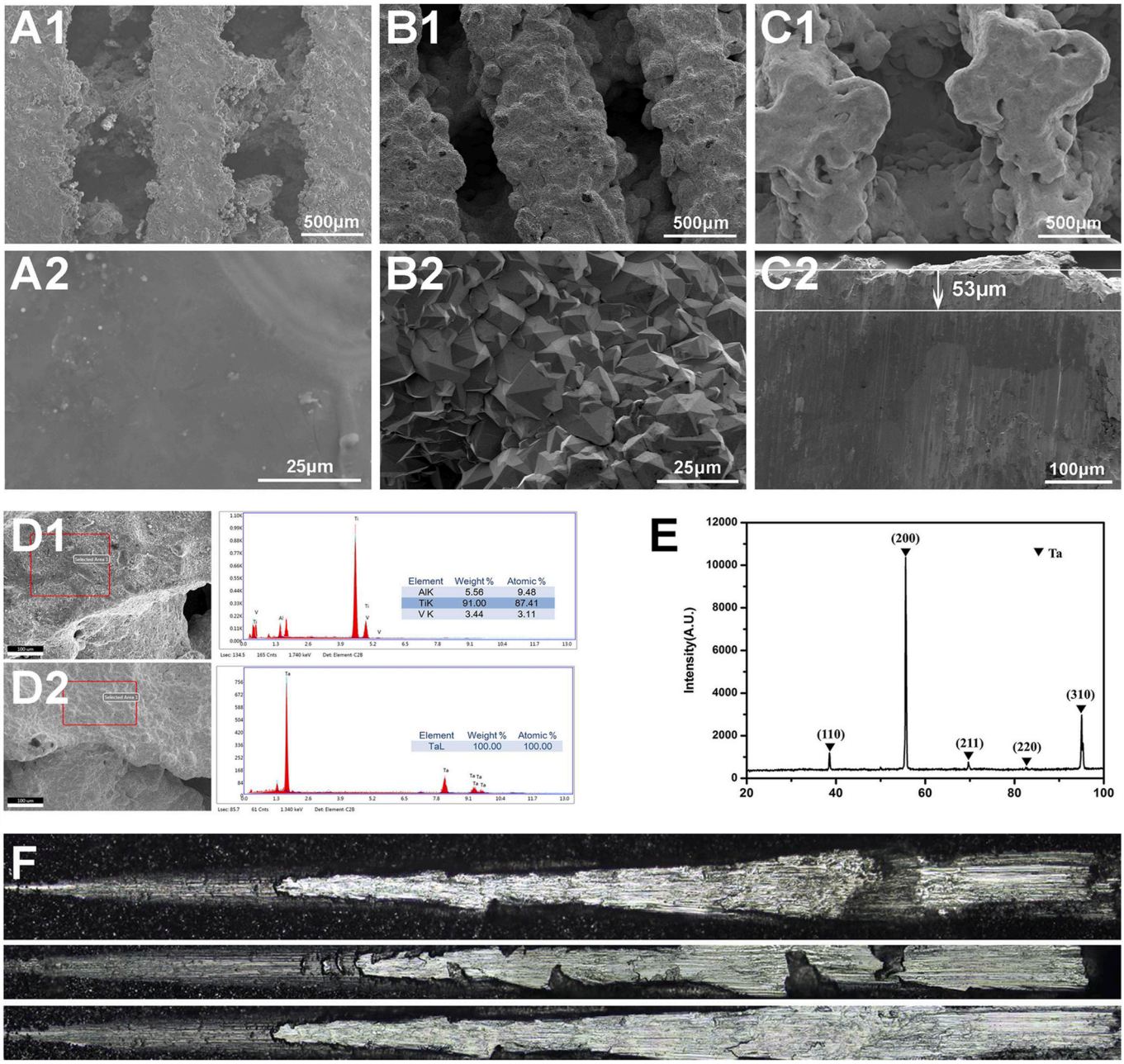

Fig. 1. SEM images of (A1, A2) pTi, (B1, B2) Ta-coated pTi, and (C1, C2) the cross-section of Ta-coated pTi. EDS data for (D1) pTi, (D2) Ta-coated pTi. XRD data for (E) Ta-coated pTi. (F) Test image of adhesion force of Ta coating on solid titanium surface.

(200), (211), (220) and (310) Ta (JCPDS 04–0788) were detected at the coating. The scratch test was further performed to examine the adhesion strength of the Ta coating. The average adhesion strengths were approximately 53 ± 7.5 MPa for the Ta coating CVD on solid Ti substrates (Fig. 1 F).

3.2. Biomechanical tests

The test results of the bending performance of the three groups of bone plates are shown in Fig. 2. The maximum flexural strengths of the pTi plate and Ta-coated pTi plate were 284 MPa and 329 MPa (Fig. 2 A), respectively. The maximum tensile strength of pTi plate and Ta-coated pTi plate are 195 MPa and 236 MPa respectively (Fig. 2 B), and the elastic modulus of the pTi plate and Ta-coated pTi plate were 53 GPa and 64 GPa, respectively.

3.3. Biocompatibility evaluation

MG-63 human osteoblasts were co-cultured with pTi and Ta-coated pTi scaffolds, respectively. The adhesion and proliferation of cells on the scaffolds were observed using SEM. After 3 days of co-cultivation, the cells were observed adhering to the pTi and Ta-coated pTi surfaces (supplementary materials: Fig. S1 A and C), but more cells grow on the Ta-coated pTi surface. Cell adhesion was observed in the pTi and Ta-coated pTi porous pores (supplementary materials: Fig. S1 B and D). In the Ta-coated porous structure, the cells were connected to each other through pseudopods and tightly adhered to the porous structure (supplementary materials: Fig. S1 D). These results indicate that the rough surface morphology of the tantalum coating is beneficial to cell adhesion and proliferation.

3.4. Fracture healing and callus formation by radiographic assessment

No infection or rejection reactions occurred at the surgical site in the experimental animals. One animal died due to anaesthesia. Another animal experienced internal fixation failure due to loosening of the non-weight-bearing brace in 3 weeks after surgery and struggling, resulting in weight-bearing and uneven stress. A corresponding replacement was carried out. Standardized anterior-posterior and lateral-medial radiographic follow-up images of all groups were performed every four weeks to document and score the healing process. The osteotomy site, the osteotomy space, and the steel plate and screw site were generally identical. At 4 weeks after surgery, the three groups showed good fracture fixation with no displacement and a clear fracture line. In the pTi groups and the Ta coating groups, the formation of callus tissue was seen around the fracture, but in the Ti groups, almost no callus growth was observed in areas around and opposite the bone plate (Fig. 3 A1, B1 and C1). At 8 weeks after surgery, the three groups showed good fracture fixation with no displacement and the fracture line was still visible. Large amounts of callus growth were observed in areas around and opposite the bone plate (Fig. 3 A2, B2 and C2). At the 12 weeks, the fracture of the Ta coating groups was healed, the fracture line disappeared, the bone density at the fracture site increased, the growth of the callus around and on the opposite side of the bone plate decreased, and the medullary cavity was basically unobstructed (Fig. 3C3). However, despite the formation of callus in the Ti groups and pTi groups, the fracture line still exists (Fig. 3 A3 and B3). At the 16 weeks, the fracture in the Ta coating groups was completely healed, the bone plasticity was good, and the medullary cavity was completely recanalized (Fig. 3C4). The fractures in the Ti and pTi groups were healed, but hardened bone was found around the fracture, and the callus was not completely plasticity (Fig. 3 A4 and B4). At 4, 8, 12, and 16 weeks after surgery, the Lane-Sandhu score of the porous Ta coated plate groups was higher than that of the Ti plate groups and the pTi plate groups, and the difference was statistically significant ($P < 0.05$) (Fig. 3 D).

Micro-CT scans were performed to obtain data from each groups at 4, 8, 12 and 16 weeks after surgery. The micro-CT images showed fracture healing more accurately than the X-ray images. A large amount of callus formation was observed in the Ti plate groups at 8 weeks after surgery, but the fracture line was still obvious (Fig. 4 B). At 12 weeks after surgery, the fracture line was blurred, and the callus began to mould (Fig. 4C). The fracture line disappeared completely at 16 weeks after surgery (Fig. 4 D). A 3D image showed callus hypertrophy in the fracture site of the Ti plate groups (Fig. 4 A1-D1). The callus hypertrophied during the fracture healing process in the pTi plate groups (Fig. 4E–H). After 12 weeks, the fracture line was blurred, and the callus was moulded (Fig. 4 G). The fracture line disappeared at 16 weeks after surgery (Fig. 4H). The 3D image showed callus hypertrophy at the fracture site (Fig. 4 E1-H1). The fracture line in the porous Ta-coated plate groups was blurred at 4 weeks (Fig. 4 I) and disappeared at 16 weeks (Fig. 4 L) after surgery. Callus moulding was basically completed at 12 weeks (Fig. 4 K) and was completed at 16 weeks after surgery (Fig. 4 L). The 3D images showed that the fracture was united, that the callus was non-hypertrophic and that new bone grew into the porous Ta-coated plate (Fig. 4 I1-L1).

The grey values of all groups were measured at multiple points at each time point. Each groups showed a “U"-shaped grey value curve, and among all time points, 8 weeks after the operation gave the lowest grey values (Fig. 4 M). There was no difference in the grey values between any groups at 4 weeks after surgery, and at 8 and 12 weeks after surgery, the grey values in the porous Ta-coated plate groups were significantly higher than those in the pTi and Ti plate groups ($p < 0.01$). After 16 weeks, the grey value in the porous Ta-coated plate groups was significantly higher than that in the Ti plate groups ($p < 0.01$), and the difference between the porous Ta-coated plate groups and the pTi plate groups was not statistically significant. The grey value in the porous Ta-

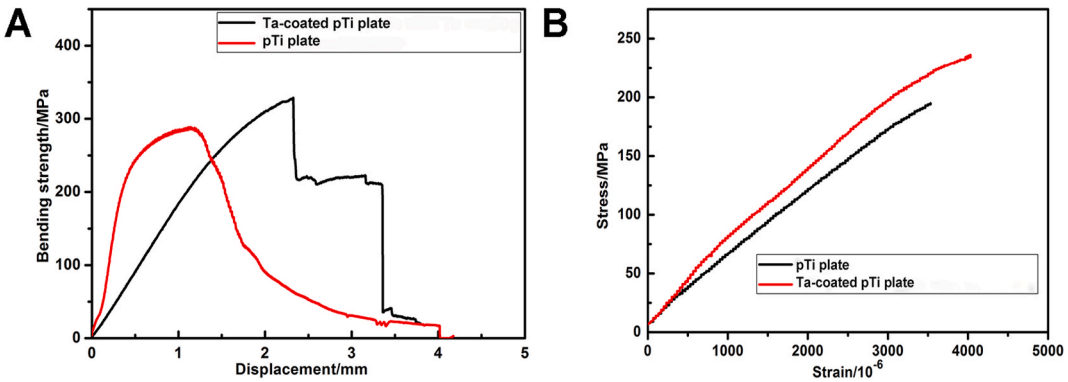

Fig. 2. The mechanical performance test of bone plates. (A) Bending strength of pTi plate and Ta-coated pTi plate. (B) Tensile Strength of pTi plate and Ta-coated pTi plate.

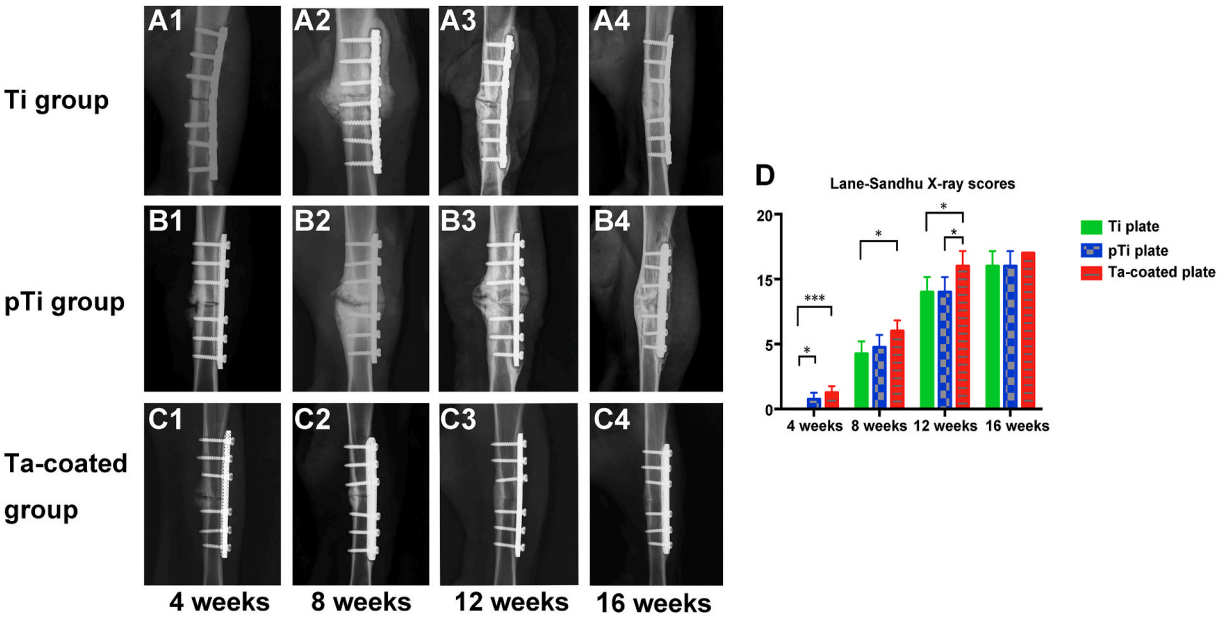

Fig. 3. X-ray observation of fracture healing state: (A1-A4) Fracture healing process in the Ti plate groups. At 12 weeks after surgery, the fractures in the normal Ti plate groups healed, but the medullary cavity did not pass. (B1–B4) A large number of calli were generated after the operation in the pTi plate groups. (C1–C4) A rapid fracture healing process was observed in the porous Ta-coated Ti plate groups, wherein the fracture healed 12 weeks after the operation and the medullary cavity was free. (D) Lane-Sandhu X-ray scores showed that fracture healing in the porous Ta-coated plate groups was better than the other two groups from 4 weeks to 12 weeks after surgery ($P < 0.05$).

coated plate groups after 12 weeks was significantly higher than the normal bone grey value ($p < 0.01$). The grey values in the porous Ta-coated and pTi groups were similar to that of normal bone at 16 weeks. Nevertheless, the grey value in the Ti plate groups was lower than the normal bone grey value ($p < 0.01$).

3.5. Histomorphological evaluation

Histomorphological evaluation was performed on a thin section of each sample in the mid-sagittal plane through the center of the bone stained with Van-Gieson stain at 4, 8, 12, and 16 weeks after surgery (Fig. 5). Four weeks post operation in the pTi plate and porous Ta-coated plate groups, fibrillar connective tissue formation was observed in the medullary cavity (Fig. 5 A and E). Moreover, new cartilage and fibrillar connective tissue grew into the pores of the porous Ta-coated plates (Fig. 5 E1 and E2). At 8 weeks after surgery, massive fibrillar connective tissues formed in the medullary cavity in the pTi and Ta-coated plate groups, and the fracture lines blurred in the two groups (Fig. 5 B and F). However, new bone tissue was observed in the pores of the porous Ta-coated plates (Fig. 5 F2). Fracture healing was found at 12 weeks post operation in the pTi and porous Ta-coated plate groups (Fig. 5C and G). Massive new bone tissue grew on the surface and into the pores of the porous Ta-coated plate (Fig. 5 G2). However, there was no new bone tissue in the pTi plate groups (Fig. 5C2). At 16 weeks after surgery, the fractures in the pTi and porous Ta-coated groups healed completely (Fig. 5 D and H). The surface of the porous Ta-coated plate was covered by new bone tissue, and the pores were covered with new bone tissue (Fig. 5H2 and H3). However, this phenomenon did not occur on the surface of or inside the pTi plate (Fig. 5 D2 and D3). Due to the high hardness of the Ti tibia plate, we did not complete the hard tissue section of the Ti groups, which was very unfortunate in this manuscript.

3.6. SEM observation of osteocytes around bone plates

A comparison of the three groups under electron microscopy at 16 weeks post operation indicated that the porous Ta-coated plate groups had better porous structure bone growth and stronger fusion between the bone tissue and bone plate than the other groups (supplementary materials: Fig. S2). The surrounding osteocytes reside in lacunae interconnected through canalicul in the porous Ta-coated plate groups (supplementary materials: Fig. S2 C). Another surprising observation was that the Ta coating give rise to tightly interlocked lamellar bone, with osteocytes in close apposition to the coating. Moreover, the surrounding osteocytes in the porous Ta-coated plate groups had more biological activity than those in the other groups because the pseudopods are still growing towards the coating surface (supplementary materials: Fig. S2 C1).

3.7. Immunohistochemical

Immunohistochemical experiments were used to study the expression levels of BMP-2 and VEGF (supplementary materials: Fig. S3). The yellow-brown regions and yellow-brown particles are positively stained. Low levels of BMP-2 and VEGF immunological positivity were observed in osteoblasts and endothelial cells in the calluses and bone tissue around the medullary cavity in the Ti plate groups (supplementary materials: Fig. S3 A and D). In contrast, the levels of positive BMP-2 and VEGF expression in the osteoblasts and endothelial cells in the pTi plate groups were moderate, as shown by staining of the bone tissues around the calluses and the pTi fixation site. There was also a significant increase in newly formed vascular tissue, the endothelial thickness was increased, and the luminal diameter was reduced (supplementary materials: Fig. S3 B and E). In the porous Ta-coated plate groups (supplementary materials: Fig. S3 C and F), the levels of BMP-2 expression in the osteoblasts and endothelial cells in the bone tissues around the calluses and the porous Ta-coated fixation site were significantly higher than those in the other groups ($p < 0.01$). The levels of VEGF expression in the porous Ta-coated plate groups and pTi plate groups were higher than those in the Ti plate groups ($p < 0.05$) (supplementary materials: Fig. S3 G). Moreover, in the porous Ta-coated groups, there was more osteoblast differentiation and mature osteoblast aggregation, the vascular endothelium was significantly thickened, and vascularization was apparent.

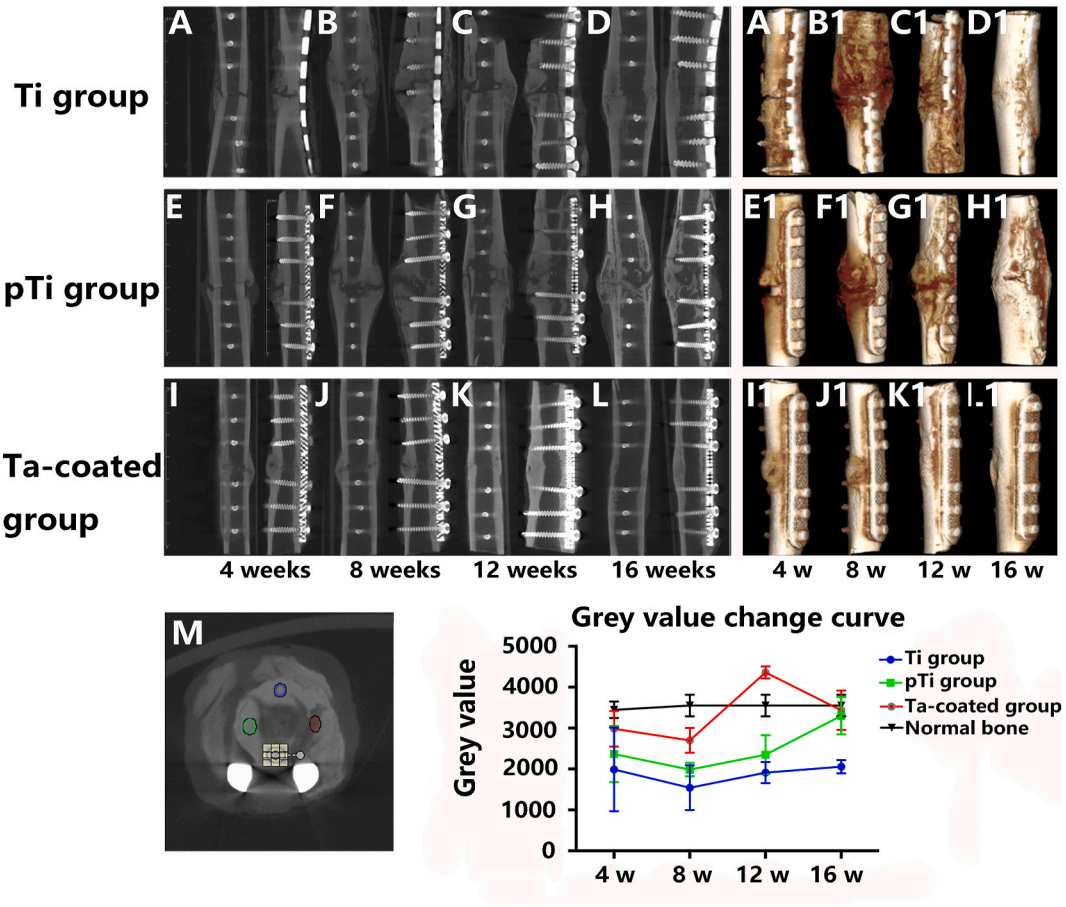

Fig. 4. Micro-CT observation of fracture healing state: Fracture healing process in the Ti plate groups (A–D). Three-dimensional image of callus hypertrophy in the fracture site of the Ti plate groups (A1-D1). Fracture healing process in the pTi plate groups (E–H). Three-dimensional image of callus hypertrophy in the pTi plate groups (E1-H1). The fracture healing process in the Ta-coated pTi plate groups (I–L). 3D image of the fracture site in the Ta-coated pTi plate groups (I1-L1). In the Ta-coated pTi plate groups, the fractures are healed, and the callus is well-shaped. The thickness of the bone cortex on both sides is the same: multi-point measurement and change curve of grey value (M).

3.8. Finite element analysis

Using HyperWorks finite element modelling software (Fig. 6 A ~ A3), as seen from the fracture location, the maximum deformation position was located at the plate edge, the maximum displacement was 0.381 mm, the maximum stress of the internal fixation system was 319.2 MPa, the maximum stress of the bone was 47.7 MPa, and the maximum strain values of the internal fixation material and bone were $-2.168e^{-3}$ and $-2.957e^{-3}$, respectively, during fracture healing in the Ti plate model (Fig. 6 B ~ B3). The pTi plate and porous Ta-coated plate models exhibited the same stress outcome. The maximum deformation position was located at the plate edge, the maximum displacement was 0.4336 mm, and the maximum stress of the internal fixation material was 551.2 MPa, and the maximum stress of the bone was 52 MPa. The maximum strain values of the plate and bone were $-4.344e^{-3}$ and $-3.215e^{-3}$, respectively, during fracture healing (Fig. 6C ~ C3). The allowable limits of the nonporous and porous internal fixation systems both meet the needs of fracture fixation (Fig. 6 D and Table 1). After the fracture healed, the maximum deformation position was located in bone in the Ti plate (Fig. 7 A ~ A3) and porous Ta-coated plate (Fig. 7C ~ C3) models, and the maximum deformation position of the pTi plate was located at the plate edge (Fig. 7 B ~ B3). The maximum stress of the internal fixation system was 115.59 MPa, 132.2 MPa and 75.5 MPa in the Ti plate model, pTi plate model and porous Ta-coated plate model, respectively (Fig. 7 D and Table 2); the maximum stress of bone in these three models was 18.87 MPa, 17.1 MPa, and 26.65 MPa, respectively (Fig. 7 D and Table 2). Stress and deformation analysis of the conventional Ti plate and porous bone plates when the fracture was not healed showed that both the porous bone plate and conventional Ti plate met the strength requirements for fixation. The Ta-coated pTi plate groups had the best bone penetration, the highest bone conduction force and the highest travel distance between the bone and bone plate. The stress could be evenly distributed in the porous plates and bone after fracture healing to avoid stress shielding and help realize long-term support (Fig. 8).

4. Discussion

The internal fixation material for clinical fracture treatment is usually composed of high-strength stainless steel and Ti alloy. The principles and techniques of the AO/ASIF Research Association emphasize surgical management of fractures, the mechanical aspects of internal fixation, and the absolute stability of fractures [24]. However, this mismatch in mechanical properties would result in uneven stress distribution, and the majority of the load is transferred by the plate rather than by the underlying bone [25]. Stress-shielding effects could lead to osteoporosis, bone resorption or atrophy, and secondary fractures [24, 26]. The poor tissue compatibility between stainless steel and Ti alloy plates may be due to corrosion of the metal implants, leading to re-fracture, and severe ionization reactions, leading to infection of the surrounding soft tissues [12]. Traditional metal bone plates have poor plastic capacity and cannot provide effective fixation in complex fractures or irregular bone shapes. The lack of adhesion between bone and plate increases the risk of fracture complications, which is not conducive to fracture healing or long-term implantation. In this context, a plate

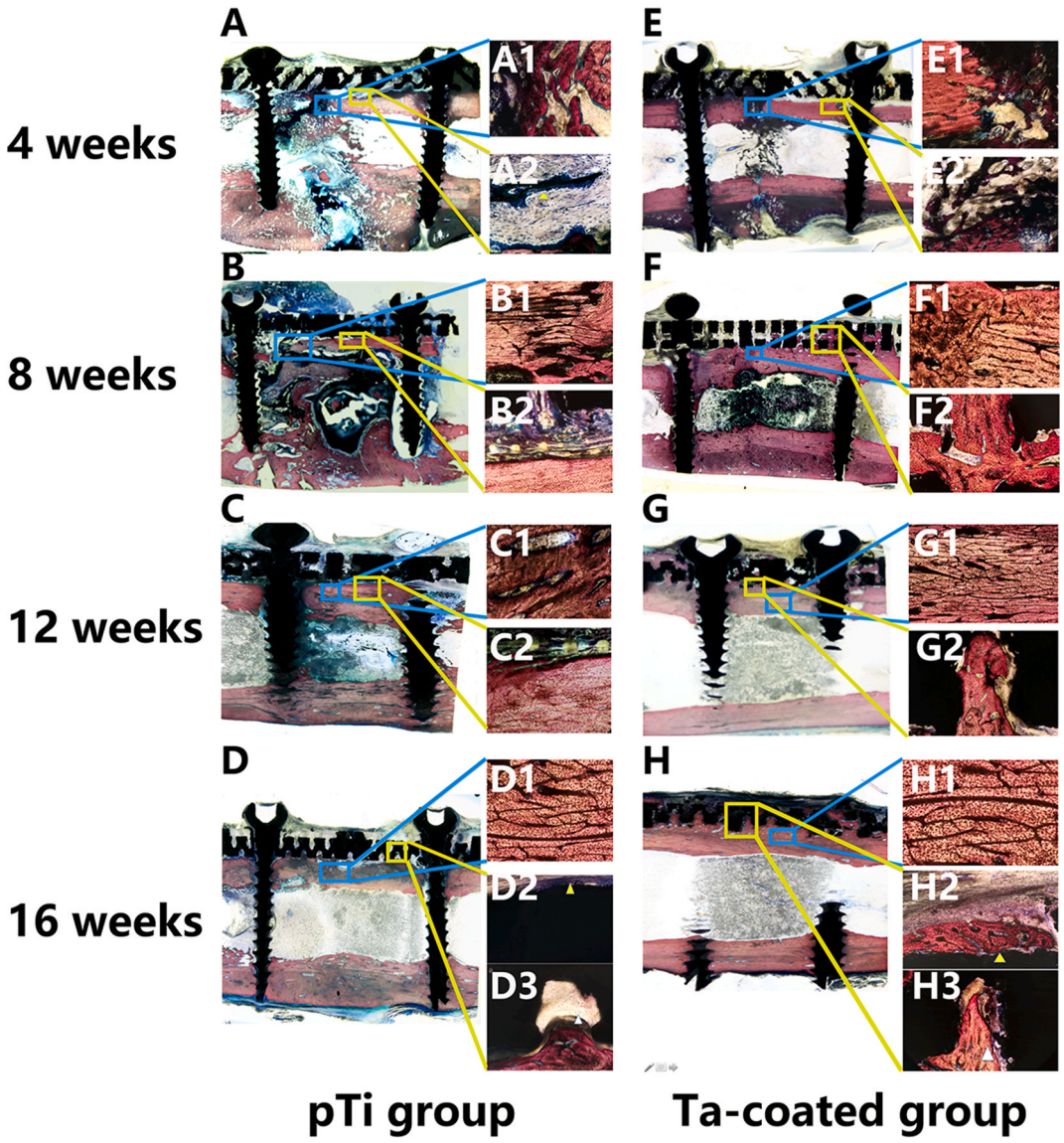

Fig. 5. Van Gieson staining to assess callus formation and the interface of the bone and plate at 4, 8, 12 and 16 weeks in the pTi groups and Ta-coated pTi groups. Upper right: healing status at the fracture gap (at × 100 magnification); Lower right: interface between the bone plate and bone (at × 100 magnification). The blue mark represents the fracture gap, and the yellow mark represents the bone plate and bone interface. (For interpretation of the references to colour in this figure legend, the reader is referred to the Web version of this article.)

suitable for long-term implantation, satisfying the requirements of individualized treatment of fractures, promoting primary healing, and avoiding stress shielding has become the focus of scientists and orthopaedic surgeons. To date, however, there have been no impressive results with regard to new fixation devices.

The goal of this research is to produce a personalized bone plate that has promising mechanical strength and low elastic modulus, which can effectively fix fractures without stress shielding; meanwhile, the bone plate also has better biological activity, promote fracture healing, and can stay in the body for a long time. In this study, an electron beam melting method was used to prepare personalized pTi bone plates, and then CVD technology was used to coat Ta metal on the pTi bone plates. The prepared pTi bone plate has a pore size of 600 ± 27 μm and a porosity of about 75%. The porous Ta-coated bone plate has a pore size of 550 ± 42 μm and a porosity of about 70%. Previously some studies [27–29] have shown that biomaterials with specific porous structures can induce new bone formation at non-bone sites without the need for osteoinductive biomolecules. Compared with non-porous materials, biomaterials with a pore size of about 500 μm are more conducive to cell adhesion, diffusion, proliferation, and differentiation, promoting bone formation and capillary formation. Therefore, it can accelerate the repair of bone defects. The interconnected porous structure provides a protected area without strong fluid movement, thereby providing enough space for cells to differentiate along the osteogenic lineage [30]. Fukuda et al. [31] reported that when the pore size is 500 μm, the optimum balance between the vasculature, the availability of calcium and phosphate ions, and fluid movement is more osteoinductive. After tantalum coating, the coefficient of friction on the outer surface of the bone plate is 40% ~ 80% higher than other surface-treated materials, which is a natural product of CVD technology [32]. The high friction coefficient can promote the close adhesion of cells and tissues to the implant, promote the adsorption of macromolecular substances on cells and bone tissue, and enhance the strength of the connection between the scaffold and bone tissue, forming a good coating interface first step.

The purity and bonding strength of the coating is critical parts of developing a good interface. EDS and XRD test results prove that the purity of the Ta coating is 100%, and the high-purity tantalum coating can maintain long-term chemical stability after being implanted in the

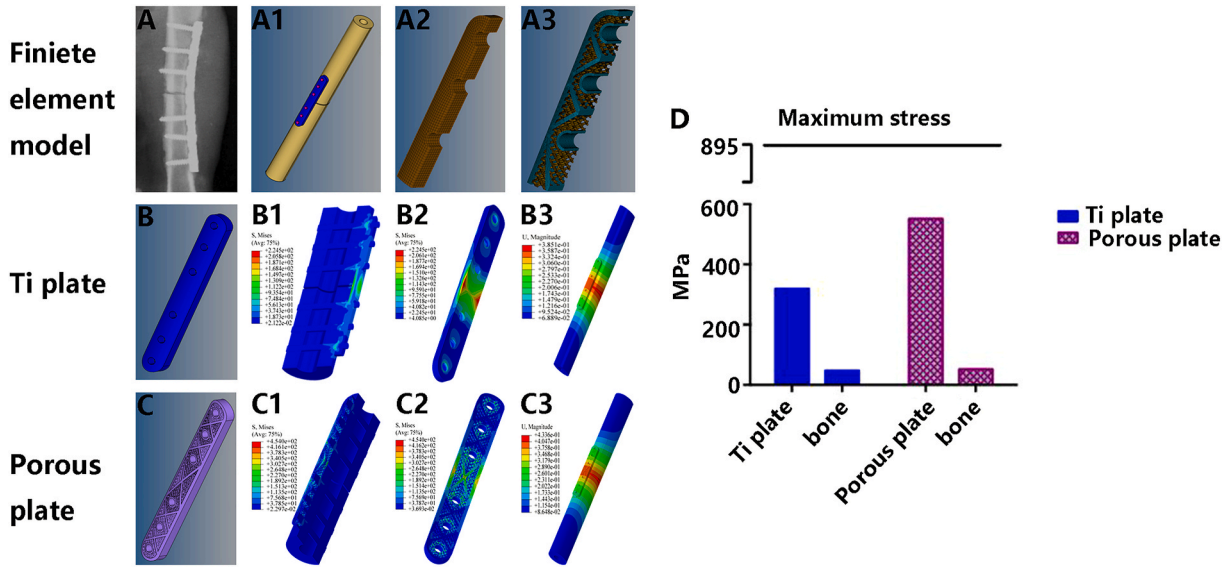

Fig. 6. Finite element analysis during fracture healing: radiograph of the fracture fixation (A), fracture fixation model (A1), the internal structure of the Ti plate model (A2), the internal structure of the porous plate model (A3). Ti plate fixation model during fracture healing: Ti plate model (B), the stress nephogram of the bone and internal fixation system (B1), the stress nephogram of the Ti plate (B2), the strain nephogram of the bone, and internal fixation system (B3). Porous plate fixation model during fracture healing: porous plate model (C), the stress nephogram of the bone and porous internal fixation system (C1), the stress nephogram of the porous plate (C2), the strain nephogram of the bone and porous internal fixation system (C3). (D) Stress analysis.

Table 1
Finite element analysis of the internal fixation system and bone during fracture healing.

Working condition (fracture unhealed)>	Maximum deformation position	Maximum displacement/mm	Parts	Maximum stress (material)/MPa	Maximum strain	Allowable limit of the material/MPa
Ti plate	Fracture location	0.3851	material	319.2	$-2.168e^{-3}$	895 (TC-4)
			Bone	47.7	$-2.957e^{-3}$	(170)
pTi plate	Plate edge	0.4336	material	551.2	$-4.344e^{-3}$	895 (TC-4)
			Bone	52	$-3.215e^{-3}$	(170)
Ta-coated pTi plate	Plate edge	0.4336	material	551.2	$-4.344e^{-3}$	895 (TC-4)
			Bone	52	$-3.215e^{-3}$	(170)

body. Coating adhesion is a prerequisite for forming a good interface and should be resolved before clinical application. The test results show that the average critical load value of the Ta coating from the Ti solid planar substrate is 53 ± 7.5 MPa. At present, the ISO standard for hydroxyapatite coatings is that the bond strength must be greater than 15 MPa [33]. The adhesion strength of Ta coating is much higher than hydroxyapatite coating on titanium-based metal with a bonding strength of 15 ~ 25 MPa required for clinical applications [34]. Excellent coating adhesion can effectively prevent the implant coating from delamination in the body, reducing the possibility of long-term relaxation and infection of the implant.

Osteoblast differentiation is the premise and basis of the formation of dominant osteogenesis in the process of osteogenesis differentiation. Osteoblast differentiation is the most basic biological characteristic in bone matrix synthesis, secretion, mineralization and maturity. In vitro experiments show that the rough surface morphology of the tantalum coating contributes to cell adhesion and proliferation. This finding is consistent with previous research results [35,36].

Excellent mechanical properties are vital for metal implant materials to be used as fracture internal fixation implants. The mechanical test results show that both pTi bone plates and tantalum-coated pTi bone plates have excellent flexural strength and low elastic modulus. While satisfying the good mechanical properties of the implant material, it can effectively avoid the adverse effects caused by stress shielding. The results of continuous X-ray examination showed that the three groups of bone plates could firmly fix the fracture without breaking, which further verified that the three groups of bone plates have good mechanical properties. Lane-Sandhu X-ray scoring system and CT grey value were used for various animal fracture models and efficacy evaluation. In the goat fracture model, we found that the Lane-Sandhu X-ray score and grey value of the porous Ta coating groups were higher than the Ti plate group and the pTi plate groups at 4, 8, 12, and 16 weeks after internal fixation. This result shows that Ta coating promotes fracture healing, which was consistent with the in vitro test results.

An analysis of hard tissue sections showed a comparison of bone penetration between the pTi plate groups and porous Ta-coated plate groups from 4 to 16 weeks after surgery. Four weeks after surgery, the fracture haematoma in the pTi plate groups intensified to form fibrous granulation tissue, and the fracture was preliminarily connected. Moreover, the internal and external membranes of the bone proliferated into osteoid tissue and extended to the fracture site. However, the porous Ta-coated plate groups not only completed haematoma activation but also contained osteoid tissue calcification inside the porous structure. On the 8th week after the operation, the calcification of fibrous tissue with a porous structure grew into the pTi plate as cartilage tissue, and new bone appeared in the porous structure of the porous Ta-coated plate. Twelve weeks after surgery, new bone appeared in the porous structure of the pTi plate, and the callus of the porous Ta-coated plate was strengthened 16 weeks after fixation surgery. The surrounding bone tissues and the internal fixation systems were tightly fused, and the porous Ta-coated structure was filled with newly synthesized bone tissue. In comparison, the pTi did not tightly fuse with the bone tissues. We observed that the porous Ta-coated internal fixation system with the bone formed a uniform bone-to-plate complex after fracture healing,

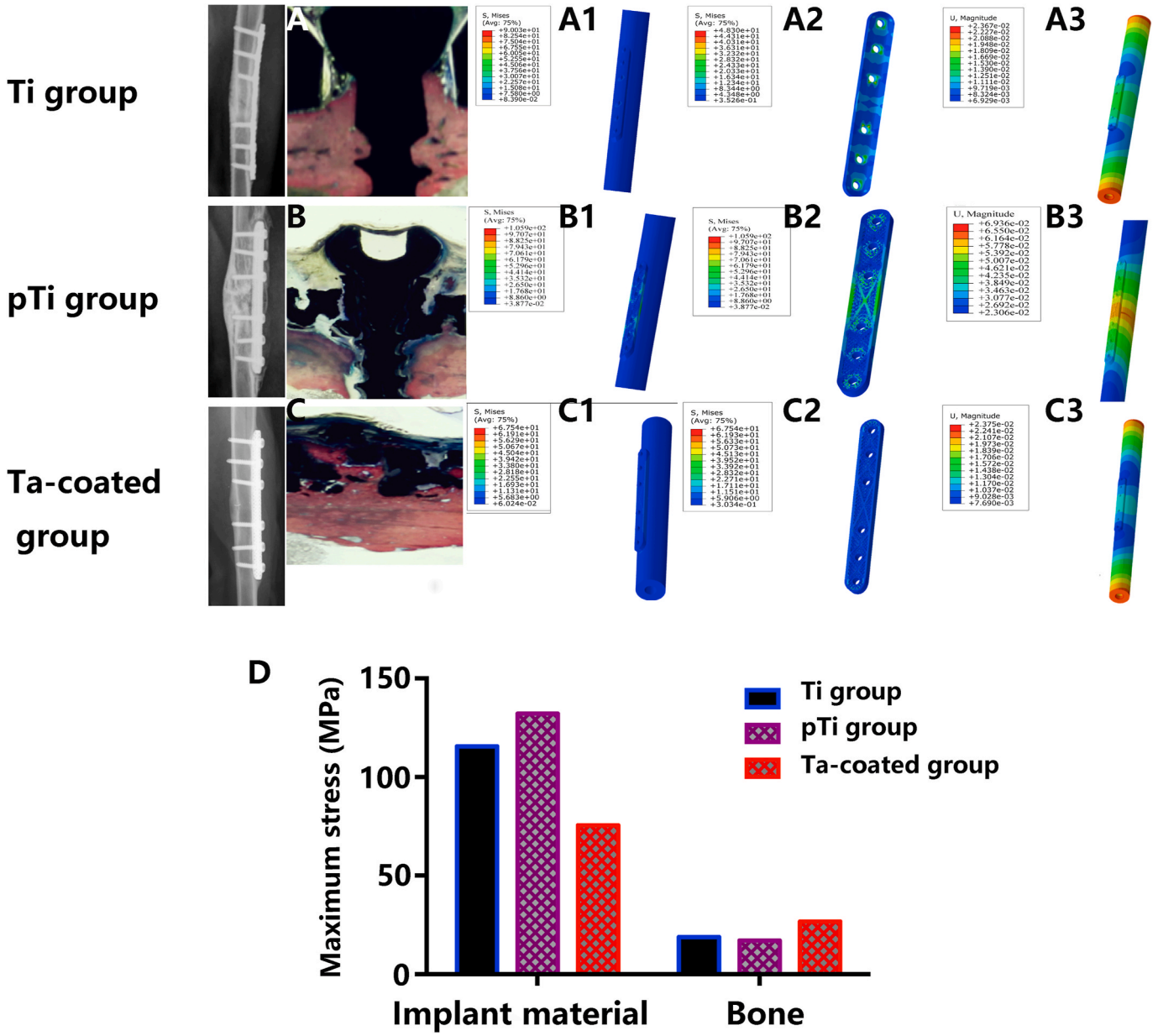

Fig. 7. Finite element analysis after fracture healing: Ti plate fixation model after fracture healing: radiographs and hard tissue section of the Ti internal fixation system (A), the stress nephogram of the bone and Ti internal fixation system (A1), the stress nephogram of the Ti plate (A2), the strain nephogram of the bone and Ti internal fixation system (A3). PTi plate fixation model after fracture healing: radiographs and hard tissue section of the pTi internal fixation system (B), the stress nephogram of the bone and pTi internal fixation system (B1), the stress nephogram of the pTi plate (B2), the strain nephogram of the bone and pTi internal fixation system (B3). Ta-coated pTi plate fixation model after fracture healing: radiographs and hard tissue section of the porous Ta-coated internal fixation system (C), the stress nephogram of the bone and porous Ta-coated internal fixation system (C1), the stress nephogram of the porous Ta-coated plate (C2), the strain nephogram of the bone and porous Ta-coated internal fixation system (C4). (D) Stress analysis.

Table 2
Finite element analysis of the internal fixation system and bone after fracture healing.

Working condition (fracture healed)	Maximum deformation position	Maximum displacement/mm	Parts	Maximum stress/MPa	Maximum strain	Allowable limit of the material/MPa
Ti plate	Bone location	0.0236	material	115.59	$1.855e^{-4}$	895 (TC-4)
			Bone	18.87	$5.505e^{-4}$	(170)
pTi plate	Plate edge	0.0694	material	132.2	$-1.161e^{-3}$	895 (TC-4)
			Bone	17.1	$-1.059e^{-3}$	(170)
Ta-coated pTi plate	Bone location	0.0237	material	75.5	$4.377e^{-4}$	895 (TC-4)
			Bone	26.65	$1.905e^{-3}$	(170)

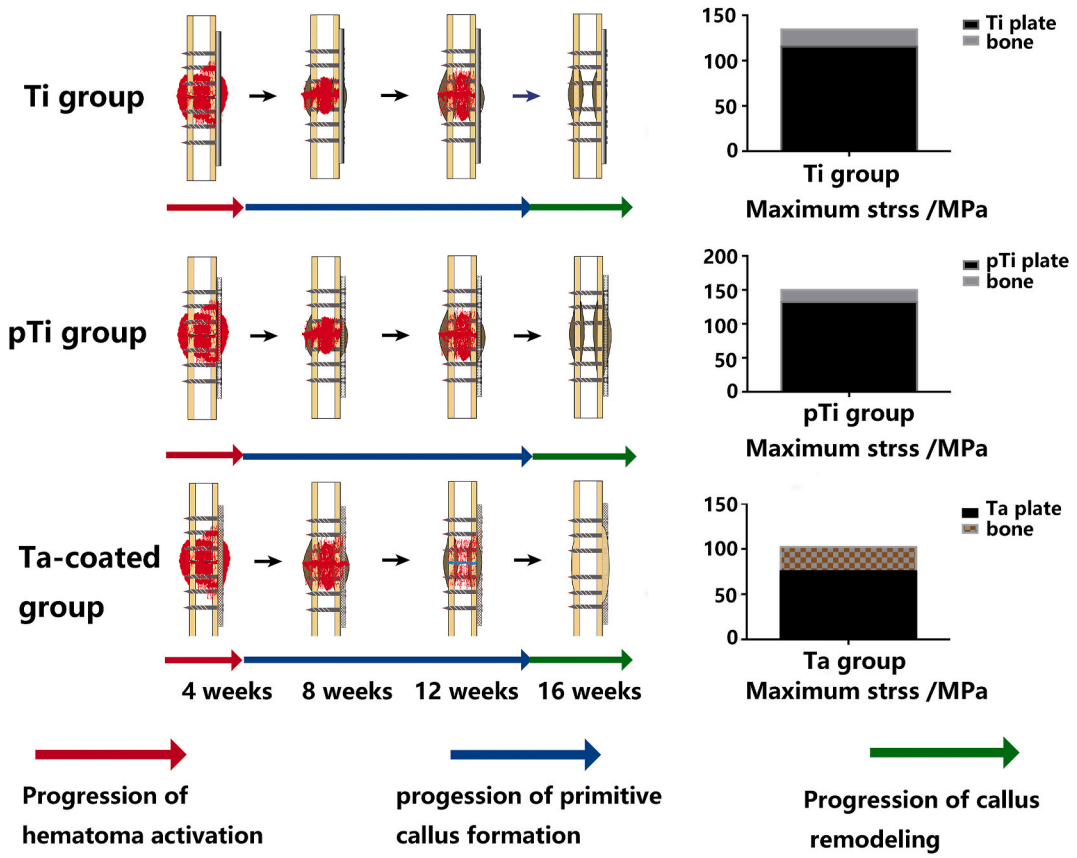

Fig. 8. Fracture healing process and mechanical conduction analysis after fracture healing. Red arrow: Progression of haematoma activation; Blue arrow: Progression of primitive callus formation; Green arrow: Progression of Callus remodelling. The porous Ta-coated plate exhibited a shorter progression of primitive callus formation and quicker fracture healing than the other plate groups. After fracture healing, the stress can be evenly distributed in the porous Ta-coated plate and bone to avoid stress shielding, achieving long-term support. (For interpretation of the references to colour in this figure legend, the reader is referred to the Web version of this article.)

which was significantly different from the structure with obvious gaps between the pTi plate or Ti plate and bone. From this result, we speculate that after the bone and porous Ta-coated plate have intergraded, a force is transmitted through the bone plate and inside the bone in mechanical conduction, which can decrease stress shielding and prevent bone absorption or bone atrophy.

Fracture healing is an extremely complex process [37]. Currently, many types of bone growth factors, such as BMP and VEGF, are isolated from bone matrices, bones, and osteocyte culture media [38,39]. BMP is a group of multifunctional cytokines that has functions, such as inducing interstitial cell migration, proliferation, differentiation, and ultimately cartilage and bone formation [40]. Previous studies have demonstrated that the local cumulative dose of BMPs must exceed a certain threshold before it can effectively induce bone formation and that low BMP concentrations are ineffective [38,39,41]. We found that at 8 weeks post operation, the BMP expression levels in the porous Ta-coated plate groups were consistently higher than those in the other two groups, which is more conducive to bone formation at the fracture site. In this study, the VEGF expression levels in the porous Ta-coated plate groups at the various time points tested were significantly higher than those in the other two groups. VEGF is an important factor that can specifically promote the growth of endothelial cells in blood vessels and induce angiogenesis [40]. This factor also plays an important role during bone healing. Studies have proven that the use of exogenous VEGF can produce earlier and longer expression of BMP at the fracture site. VEGF has important effects on BMP expression and may be one of the most important activation signals and factors for BMP expression at the fracture site [42].

Although the Ta-coated pTi plate is not hard as the Ti metal plate, even if it is used alone for bones that bear a large load. The Ta-coated pTi plate can mainly allow the bone to endure the loads after completing bone formation by starting the use without loading and gradually increasing the load level to keep pace with the progression of a bone union. At this stage, the bone tissue entered the space between the Ta-coated pTi plates, providing unity between the Ta-coated pTi plate and the stratum bone. The finite element model further verified that the bone in the porous Ta-coated plate model shared more stress after the fracture healed. The stress could be evenly distributed in porous Ta-coated plates and bone after fracture healing to avoid stress shielding and help realize long-term support.

5. Conclusion

In this research, we first prepared a porous structure composed of thin-walled Ti metal similar to the structure of human cancellous bone through a 3D printing process and then used CVD technology to coat bioactive Ta metal on the pTi bone plate. In vivo implantation experiments have proven that the bone plate can fix fractures and will not produce stress shielding. Compared with traditional metal bone plates, this new bone plate can promote fracture healing, and after long-term implantation, the structure can be integrated into the host bone without negative impact on the bone tissue, with no need for removal. These current results prove the feasibility and effectiveness of the porous Ta-coated bone plate, and it is a potential internal fixation device for fractures.

CRediT authorship contribution statement

Baoyi Liu: Formal analysis, Designed the study, wrote the animal ethical approval and the manuscript; performed all data collection and analysis; prepared figures. **Zhijie Ma:** Writing – original draft, Used the CVD technique to prepare the porous Ta-coated internal fixation systems; performed animal care, surgeries, biomechanical tests, and contributed to manuscript writing. **Junlei Li:** Formal analysis, Writing – original draft, Designed and 3D-printed pTi plates, performed SEM imaging, analysed the porous Ta-coated plates, and contributed to manuscript writing. **Hui Xie:** Formal analysis, Histological analysis and interpretation. **Xiaowei Wei:** Formal analysis, RT-PCR analysis and interpretation. **Benjie Wang:** Formal analysis, Radiographic analysis and interpretation, and image preparation. **Simiao Tian:** Formal analysis, Writing – original draft, Performed the statistical design and analysis and contributed to manuscript writing. **Jiahui Yang:** provided support in histological preparation and data collection. **Lei Yang:** Formal analysis, Radiographic analysis and interpretation, and image preparation. **Liangliang Cheng:** Formal analysis, Histological analysis and interpretation. **Lu Li:** Formal analysis, RT-PCR analysis and interpretation. **Dewei Zhao:** Conceptualization, Supervision, He was responsible for the study design and concept; supervised study performance, evaluation, raised external funds; and revised the manuscript..

Acknowledgments

This work was supported by the Dalian Science and Technology Innovation Fund Project (No. 2018J11CY030).

Appendix A. Supplementary data

Supplementary data to this article can be found online at https://doi.org/10.1016/j.bioactmat.2021.09.009.

References

[1] H.K. Uhthoff, P. Poitras, D.S. Backman, Internal plate fixation of fractures: short history and recent developments, J. Orthop. Sci. 11 (2006) 118–126.
[2] R. Mugnai, L. Tarallo, F. Capra, F. Catani, Biomechanical comparison between stainless steel, titanium and carbon-fiber reinforced polyetheretherketone volar locking plates for distal radius fractures, Orthop Traumatol Surg Res 104 (2018) 877–882.
[3] T.Y. Wei, J.C. Huang, C.Y. Chao, L.L. Wei, M.T. Tsai, Y.H. Chen, Microstructure and elastic modulus evolution of TiTaNb alloys, J Mech Behav Biomed Mater 86 (2018) 224–231.
[4] S. Guo, Q. Meng, X. Zhao, Q. Wei, H. Xu, Design and fabrication of a metastable β-type titanium alloy with ultralow elastic modulus and high strength, Sci. Rep. 5 (2015) 14688.
[5] L. Shi, L. Wang, Y. Duan, W. Lei, Z. Wang, J. Li, et al., The improved biological performance of a novel low elastic modulus implant, PloS One 8 (2013), e55015.
[6] L. Tian, Y. Sheng, L. Huang, D.H. Chow, W.H. Chau, N. Tang, et al., An innovative Mg/Ti hybrid fixation system developed for fracture fixation and healing enhancement at load-bearing skeletal site, Biomaterials 180 (2018) 173–183.
[7] B. Su, D. Jiang, Progress of biodegradable internal fixation materials, Zhongguo Xiu Fu Chong Jian Wai Ke Za Zhi 23 (2009) 1388–1392.
[8] I.H. Beiser, I.O. Kanat, Biodegradable internal fixation. A literature review, J. Am. Podiatr. Med. Assoc. 80 (1990) 72–75.
[9] D. Zhao, Y. Huang, Y. Ao, C. Han, Q. Wang, Y. Li, et al., Effect of pore geometry on the fatigue properties and cell affinity of porous titanium scaffolds fabricated by selective laser melting, J Mech Behav Biomed Mater 88 (2018) 478–487.
[10] Z. Ma, H. Xie, B. Wang, X. Wei, D. Zhao, A novel Tantalum coating on porous SiC used for bone filling material, Mater. Lett. 179 (2016) 166–169.
[11] X. Pei, L. Wu, C. Zhou, H. Fan, M. Gou, Z. Li, et al., 3D Printed Titanium Scaffolds with Homogeneous Diamond-like Structures Mimicking that of the Osteocyte Microenvironment and its Bone Regeneration Study, Biofabrication, 2020.
[12] M. Bermúdez, F. Carrión, G. Martínez-Nicolás, R. López, Erosion–corrosion of stainless steels, titanium, tantalum and zirconium, Wear 258 (2005) 693–700.
[13] J. Helsen, YannisY. Missirlis, Biomaterials - a tantalus experience, M. Today 14 (2011), 230-230.
[14] M.S. Patel, J.R. McCormick, A. Ghasem, S.R. Huntley, J.P. Gjolaj, Tantalum: the next biomaterial in spine surgery? J Spine Surg 6 (2020) 72–86.
[15] H. Wang, J. Li, H. Yang, C. Liu, J. Ruan, Fabrication, characterization and in vitro biocompatibility evaluation of porous Ta-Nb alloy for bone tissue engineering, Mater Sci Eng C Mater Biol Appl 40 (2014) 71–75.
[16] V.K. Balla, S. Bodhak, S. Bose, A. Bandyopadhyay, Porous tantalum structures for bone implants: fabrication, mechanical and in vitro biological properties, Acta Biomater. 6 (2010) 3349–3359.
[17] J.O. Smith, B.G. Sengers, A. Aarvold, E.R. Tayton, D.G. Dunlop, R.O. Oreffo, Tantalum trabecular metal - addition of human skeletal cells to enhance bone implant interface strength and clinical application, J Tissue Eng Regen Med 8 (2014) 304–313.
[18] Z. Ma, J. Li, F. Cao, J. Yang, R. Liu, D. Zhao, Porous silicon carbide coated with tantalum as potential material for bone implants, Regen Biomater 7 (2020) 453–459.
[19] L. Yan, S. Wei, X. Cheng, Z. Tao, C. Cheng, Technology, Corrosion behavior and surface characterization of tantalum implanted TiNi alloy, Sufr Coat Tech 202 (2007) 3017–3022.
[20] X. Wang, Z. Zhu, H. Xiao, C. Luo, X. Luo, F. Lv, et al., Three-dimensional, MultiScale, and interconnected trabecular bone mimic porous tantalum scaffold for bone tissue engineering, ACS Omega 5 (2020) 22520–22528.
[21] J.F. Blanco, F.M. Sánchez-Guijo, S. Carrancio, S. Muntion, J. García-Briñon, M. C. del Cañizo, Titanium and tantalum as mesenchymal stem cell scaffolds for spinal fusion: an in vitro comparative study, Eur. Spine J. 20 (2011) 353–360.
[22] ISO 9585, Implants for Surgery-Determination of Bending Strength and Stiffness of Bone Plates, 1990. https://www.iso.org/standard/17351.html.
[23] ISO 18437-5, Mechanical Vibration and Shock-Characterization of the Dynamic Mechanical Properties of Visco-Elastic Materials-Part 5: Poisson Ratio Based on Comparison between Measurements and Finite Element Analysis, 2011. https://www.iso.org/standard/50428.html.
[24] K.S. Stiffler, Internal fracture fixation, Clin. Tech. Small Anim. Pract. 19 (2004) 105–113.
[25] S. Benli, S. Aksoy, H. Havitcioğlu, M. Kucuk, Evaluation of bone plate with low-stiffness material in terms of stress distribution, J. Biomech. 41 (2008) 3229–3235.
[26] A.R. Socci, N.E. Casemyr, M.P. Leslie, M.R. Baumgaertner, Implant options for the treatment of intertrochanteric fractures of the hip: rationale, evidence, and recommendations, Bone Joint Lett. J 99 (2017) 128–133.
[27] A.C. Jones, C.H. Arns, A.P. Sheppard, D.W. Hutmacher, B.K. Milthorpe, M. A. Knackstedt, Assessment of bone ingrowth into porous biomaterials using MICRO-CT, Biomaterials 28 (2007) 2491–2504.
[28] K. Zhang, Y. Fan, N. Dunne N, X. Li, Effect of microporosity on scaffolds for bone tissue engineering, Regenr Biomater 5 (2018) 115–124.
[29] D. Barati, O. Karaman, S. Moeinzadeh, S. Kader, E. Jabbari, Material and regenerative properties of an osteon-mimetic cortical bone-like scaffold, Regen Biomater 6 (2019) 89–98.
[30] P. Habibovic, C.M. van der Valk, C.A. van Blitterswijk, K.D. Groot, G. Meije, Influence of octacalcium phosphate coating on osteoinductive properties of biomaterials, J. Mater. Sci. Mater. Med. 15 (2004) 373–380.
[31] A. Fukuda, M. Takemoto, T. Saito, S. Fujibayashi, M. Neo, D.K. Pattanayak, et al., Osteoinduction of porous Ti implants with a channel structure fabricated by selective laser melting, Acta Biomater. 7 (2011) 2327–2336.
[32] J.D. Bobyn, G.J. Stackpool, S.A. Hacking, M. Tanzer, J.J. Krygier, Characteristics of bone ingrowth and interface mechanics of a new porous tantalum biomaterial, J Bone Joint Surg Br 81 (1999) 907–914.
[33] ISO 13779-2, Implants for Surgery - Hydroxyapatite - Part 2: Coatings of Hydroxyapatite, https://www.iso.org/standard/43827.html.
[34] E. Mohseni, E. Zalnezhad, A.R. Bushroa, Comparative investigation on the adhesion of hydroxyapatite coating on Ti-6Al-4V implant: a review paper, Int J Adhes 48 (2014) 238–257.
[35] B. Liu, F. Yang, X. Wei, X. Zhang, Y. Zhang, B. Wang, et al., An exploratory study of articular cartilage and subchondral bone reconstruction with bone marrow mesenchymal stem cells combined with porous tantalum/Bio-Gide collagen membrane in osteonecrosis of the Tibia head, Mater Sci Eng C Mater Biol Appl 99 (2019) 1123–1132.
[36] X. Wei, B. Liu, G. Liu, F. Yang, F. Cao, X. Dou, et al., Mesenchymal stem cell-loaded porous tantalum integrated with biomimetic 3D collagen-based scaffold to repair large osteochondral defects in goats, Stem Cell Res. Ther. 10 (2019) 72.
[37] T.A. Einhorn, L.C. Gerstenfeld, Fracture healing: mechanisms and interventions, Nat. Rev. Rheumatol. 11 (2015) 45–54.
[38] P.J. Bouletreau, S.M. Warren, J.A. Spector, Z.M. Peled, R.P. Gerrets, J. A. Greenwald, et al., Hypoxia and VEGF up-regulate BMP-2 mRNA and protein expression in microvascular endothelial cells: implications for fracture healing, Plast. Reconstr. Surg. 109 (2002) 2384–2397.
[39] G.E. Friedlaender, C.R. Perry, J.D. Cole, S.D. Cook, G. Cierny, G.F. Muschler, et al., Osteogenic protein-1 (bone morphogenetic protein-7) in the treatment of tibial nonunions, J Bone Joint Surg Am 83 (2001) S151–S158.
[40] T. Lyon, W. Scheele, M. Bhandari, K.J. Koval, E.G. Sanchez, J. Christensen, et al., Efficacy and safety of recombinant human bone morphogenetic protein-2/calcium phosphate matrix for closed tibial diaphyseal fracture: a double-blind, randomized, controlled phase-II/III trial, J Bone Joint Surg Am 95 (2013) 2088–2096.
[41] N. Ferrara, H.P. Gerber, J. LeCouter, The biology of VEGF and its receptors, Nat. Med. 9 (2003) 669–676.
[42] H.J. Seeherman, X.J. Li, M.L. Bouxsein, J.M. Wozney, rhBMP-2 induces transient bone resorption followed by bone formation in a nonhuman primate core-defect model, J Bone Joint Surg Am 92 (2010) 411–426.